

Bayesian waveform-based calibration of high-pressure acoustic emission systems with ball drop measurements

Chen Gu¹,¹ Ulrich Mok,¹ Youssef M. Marzouk,^{1,2} Germán A Prieto^{1,3},³
Farrokh Sheibani,¹ J. Brian Evans¹ and Bradford H. Hager¹

¹Earth Resources Laboratory, Department of Earth, Atmospheric, and Planetary Sciences, Massachusetts Institute of Technology, Cambridge, MA 02139, USA. E-mail: guchch@mit.edu

²Aerospace Computational Design Laboratory, Department of Aeronautics and Astronautics Massachusetts Institute of Technology, Cambridge, MA 02139, USA

³Departamento de Geociencias, Universidad Nacional de Colombia, Bogotá, Colombia

Accepted 2019 December 16. Received 2019 December 5; in original form 2019 June 24

SUMMARY

Acoustic emission (AE) is a widely used technology to study source mechanisms and material properties during high-pressure rock failure experiments. It is important to understand the physical quantities that acoustic emission sensors measure, as well as the response of these sensors as a function of frequency. This study calibrates the newly built AE system in the MIT Rock Physics Laboratory using a ball-bouncing system. Full waveforms of multibounce events due to ball drops are used to infer the transfer function of lead zirconate titanate (PZT) sensors in high pressure environments. Uncertainty in the sensor transfer functions is quantified using a waveform-based Bayesian approach. The quantification of *in situ* sensor transfer functions makes it possible to apply full waveform analysis for acoustic emissions at high pressures.

Key words: High-pressure behaviour; Inverse theory; Joint inversion; Waveform inversion; Acoustic properties.

1 INTRODUCTION

The history of acoustic emission (AE) dates back to the middle of the 20th century, before the term was coined in the work of Schofield (1961). Obert & Duvall (1942) first detected subaudible noises emitted from rock under compression and attributed these signals to microfractures in the rock. Kaiser (1950) recorded signals from the tensile specimens of metallic materials. Since the 1960s, much subsequent work has contributed to the development of AE techniques, which have been applied to diverse engineering and scientific problems (Drouillard 1987, 1996; Grosse & Ohtsu 2008).

AE is a useful tool to study the source mechanisms of ‘labquakes’ and the three-dimensional structure of samples under diverse fracturing experimental conditions (Schofield 1961; Pettitt 1998; Ojala *et al.* 2004; Graham *et al.* 2010; Stanchits *et al.* 2011; Goebel *et al.* 2013; Fu *et al.* 2015; Goodfellow *et al.* 2015; Hampton *et al.* 2015; Li & Einstein 2017; Brantut 2018). However, it is very difficult to use full waveforms of AE to infer AE source physics and sample structures, because AE amplitudes are affected by many factors (e.g. sensor coupling, frequency response of sensors, or incidence angle of ray paths) not related to the AE source or path effects. To determine the real physical meanings of the recorded AEs, careful calibration of their amplitudes is needed.

McLaskey & Glaser (2012) performed AE sensor calibration tests on a thick plate with two calibration sources (ball impact and glass capillary fracture) to estimate instrument response functions. Ono (2016) demonstrated detailed sensor calibration methods, including face-to-face, laser interferometry, Hill-Adams equation and tri-transducer methods. Yoshimitsu *et al.* (2016) combined laser interferometry observations and a finite difference modelling method to characterize full waveforms from a circular-shaped transducer source through a cylindrical sample. However, these calibration methods only work under ambient conditions, and not within a pressure vessel where rock physics experiments are sometimes carried out. To calibrate the AE amplitudes under high-pressure conditions, Kwiatek *et al.* (2014b) proposed an *in situ* ultrasonic transmission calibration (UTC) method to correct relative amplitudes under high pressure. McLaskey *et al.* (2015) developed a technique to calibrate a high-pressure AE system using *in situ* ball impact as a reference source. This design enabled the determination of absolute source parameters with an *in situ* accelerometer.

This study aims to advance these calibration methodologies by quantifying the uncertainty of sensor transfer functions using a waveform-based Bayesian approach. Instead of using the waveform of a single ball bounce, our approach is able to use the waveforms of multibounce events. Inferring an *in situ* sensor transfer function, and its associated uncertainty, makes it possible to apply full waveform

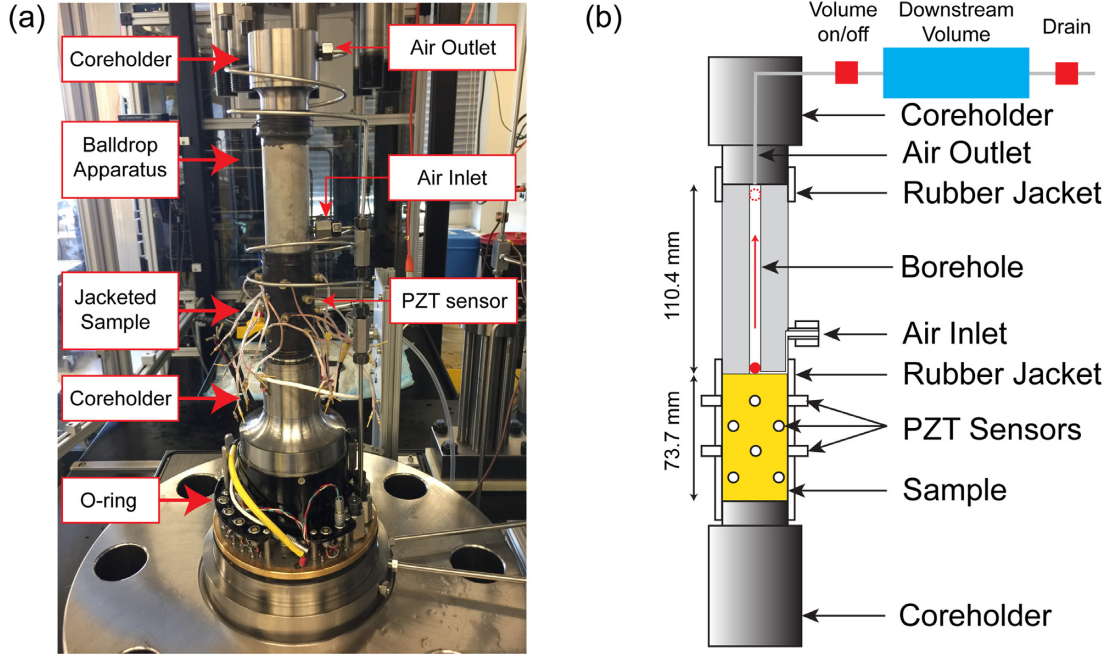


Figure 1. (a) Photo of sample assembly before closing the pressure vessel. (b) Schematic of cross-section of the ball drop apparatus and the instrumented sample.

analysis for acoustic emissions under high-pressure conditions. The method is tested using the newly built AE system of the MIT Rock Physics Laboratory.

2 METHODOLOGY

2.1 Experimental setup and AE data

The ball drop apparatus to conduct the *in situ* ball drop experiment is shown in Fig. 1. A steel ball (radius $R_1 = 3.18$ mm) placed in a tube is lifted to the top by air blown into the tube. After the air is cut off, the ball drops and hits the surface of a titanium cylinder (marked as ‘sample’ in Fig. 1), bouncing a few times. The diameter of the titanium cylinder is 46.1 mm and the length is 73.7 mm. Sixteen lead zirconate titanate (PZT) sensors are attached to the surface of the titanium cylinder (Fig. 2). We stack a non-polarized PZT piezoceramic disk, a polarized PZT piezoceramic disk, and a titanium disk adapter together to make one sensor. The diameters of the polarized and non-polarized PZT piezoceramic disks are 5.00 mm and the thicknesses are 5.08 mm. The resonance frequency is 1 MHz. The titanium disk adapter has a diameter of 5.00 mm and a thickness of 4.00 mm. The side of the titanium disk adapter contacting the polarized PZT piezoceramic disk is machined to be flat, and the other side contacting the cylindrical sample is machined to be concave, to better fit the curved cylindrical side surface. We increase the confining pressures (cp) and differential stresses (ds) gradually to improve the coupling between the PZT sensors and the sample. The *in situ* ball drop experiments are conducted at varied cp and ds. High-quality AE data are observed at: (1) cp = 10 MPa, ds = 6 MPa; (2) cp = 20 MPa, ds = 10 MPa; (3) cp = 30 MPa, ds = 10 MPa. Then we decrease both cp and ds to ambient conditions and conduct one more ball drop experiment as the baseline measurements. The ball drop experiment is conducted at

a confining pressure of 30 MPa and a differential pressure of 10 MPa.

The AE data are continuously recorded and streamed to a hard drive at a sampling rate of 12.5 MHz, preprocessed by the STA/LTA algorithm to detect events due to ball bounces (Swindell & Snell 1977; McEvilly & Majer 1982; Earle & Shearer 1994). The truncated waveforms of the first and second bounces from 16 sensors due to one ball drop experiment at cp = 30 MPa and ds = 10 MPa are shown in Fig. 2. We implement the Akaike information criterion (AIC) algorithm to automatically pick the P arrival time t_1^j for the truncated waveforms of the first bouncing event (Maeda 1985; Kurz *et al.* 2005). Then we align the waveforms from the later bounces and the first bounce by cross-correlation. An example of continuous waveforms containing the first three bouncing events of sensor 16 at cp = 30 MPa and ds = 10 MPa is shown in Fig. 3(a). The aligned waveforms of three bouncing events are shown in Fig. 3(b). The absolute P arrival time t_k^j of the k th bouncing event at sensor j can be calculated by adding the time lag between the waveforms of the first and the k th bouncing events to t_1^j . The time intervals between all the bounces recorded by sensor j can thus be collected as

$$\delta t^j = [t_2^j - t_1^j, t_3^j - t_2^j, \dots, t_{k+1}^j - t_k^j, \dots, t_n^j - t_{n-1}^j], \quad (1)$$

where n is the total number of bounces.

The same pre-processing method has also been applied to the AE data at other cp and ds. Under each conditions, we compared the waveforms at sensor 16 due to the first bounce of the ball drop at: (1) cp = 10 MPa, ds = 6 MPa; (2) cp = 20 MPa, ds = 10 MPa; (3) cp = 30 MPa, ds = 10 MPa; and (4) cp = 0 MPa, ds = 0 MPa in Fig. 4. Because higher confining pressures improve the coupling between sensors and the sample, resulting in smaller noise and larger amplitude response of sensors, the waveforms at high pressures show a smaller noise level compared to those at ambient conditions. For the same reason, the waveforms at cp = 20 MPa, ds = 10 MPa and

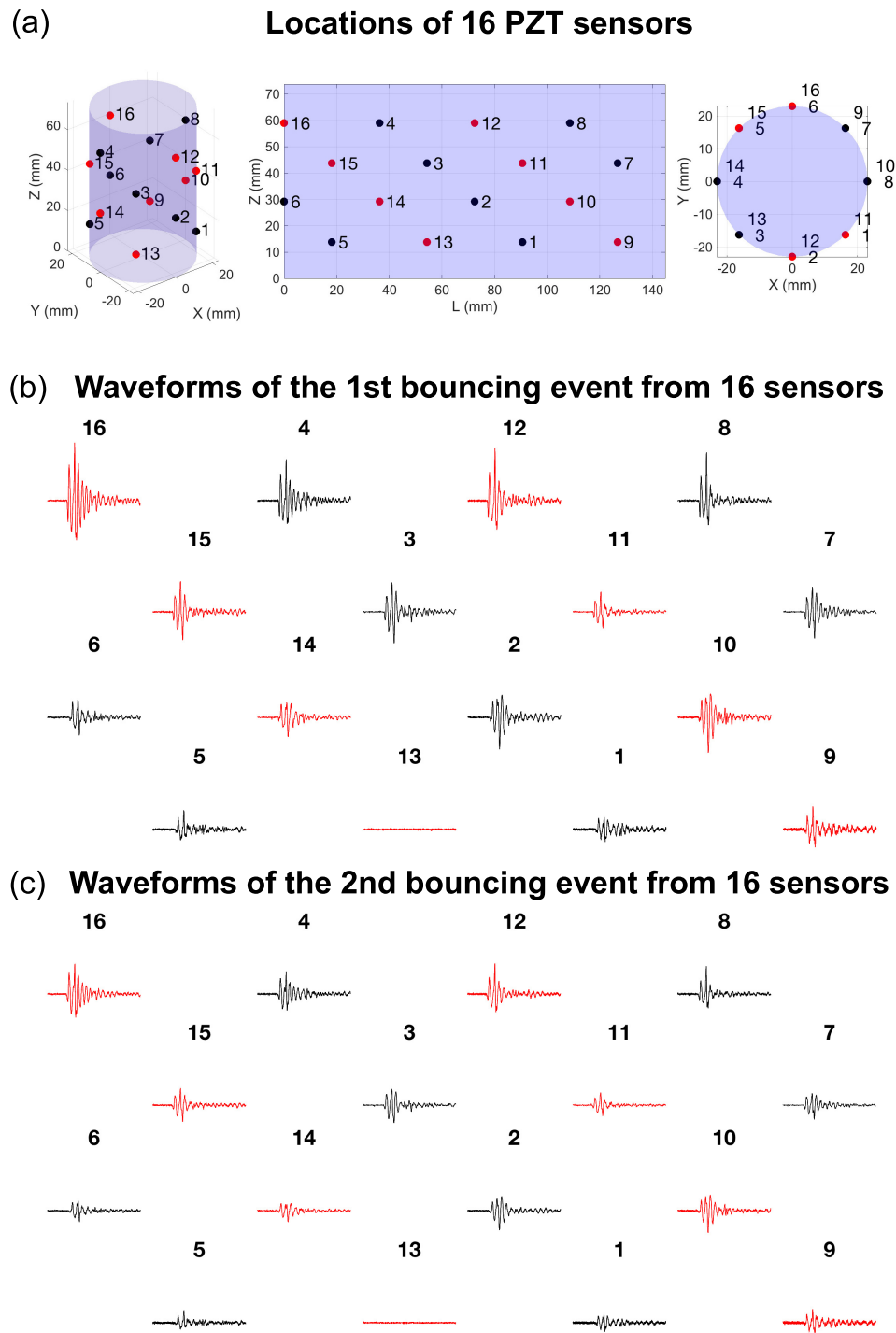


Figure 2. (a) Locations of 16 PZT sensors. (b) Example waveforms from 16 sensors for the 1st ball bounce at $cp = 30$ MPa and $ds = 10$ MPa. (c) Example waveforms from 16 sensors for the 2nd ball bounce at $cp = 30$ MPa and $ds = 10$ MPa. Black and red denote sensors and corresponding received signals on two different boards.

$cp = 30$ MPa, $ds = 10$ MPa have larger amplitudes than those at $cp = 10$ MPa, $ds = 6$ MPa. However, when the confining pressure increases beyond a critical level, higher confining pressures do not affect the noise level and sensor response, as is illustrated in the almost identical waveforms at $cp = 20$ MPa, $ds = 10$ MPa and $cp = 30$ MPa, $ds = 10$ MPa.

2.2 Bouncing time and waveform modelling

To model the time interval between bounces, we first assume that after each bounce, the rebound velocity decreases to a fraction a (the rebound coefficient) of the incident velocity; then the velocity after the k th bounce is

$$v_k = a^k v_0. \quad (2)$$

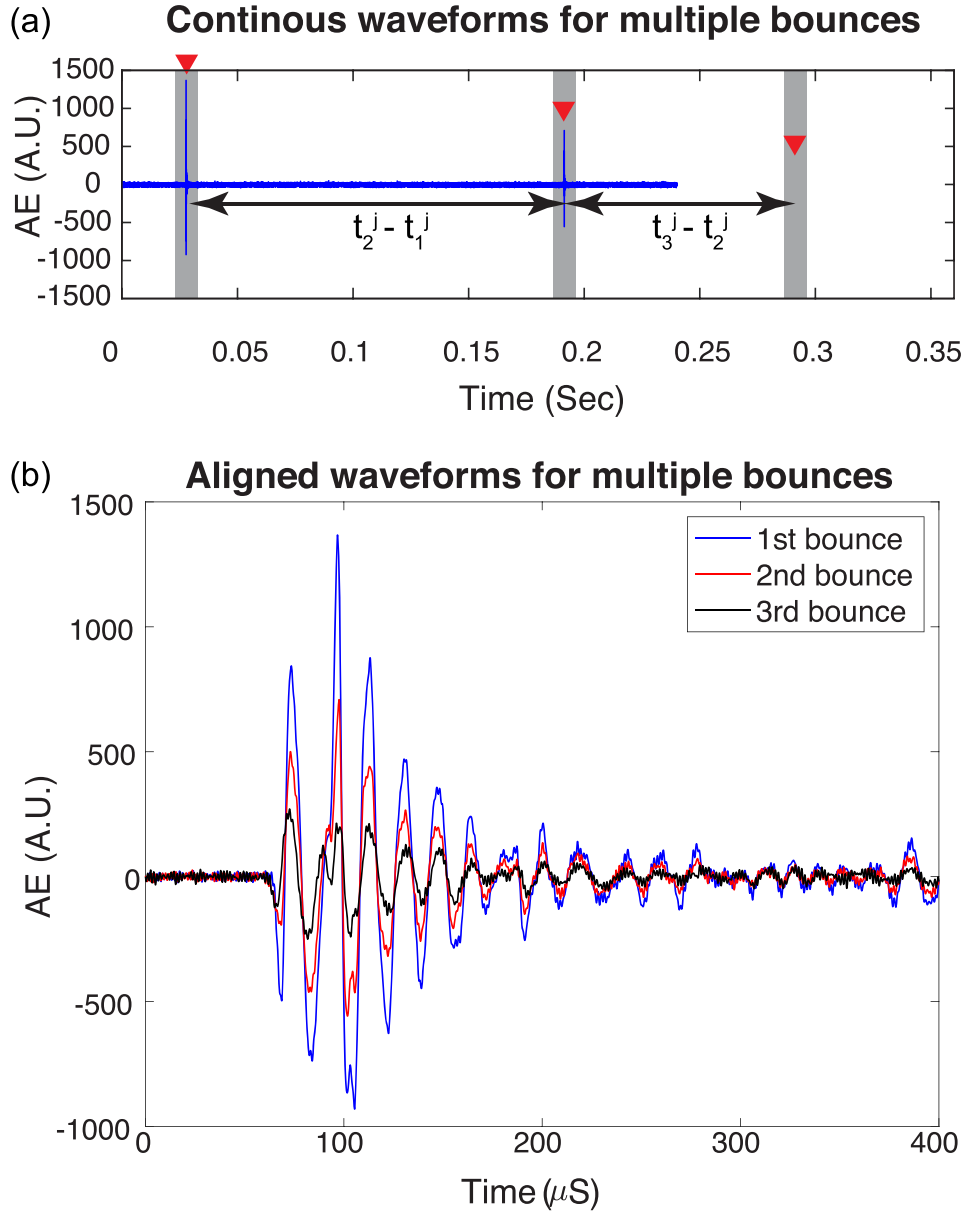


Figure 3. (a) Continuous waveforms containing the first three bouncing events of sensor 16 at $cp = 30$ MPa and $ds = 10$ MPa. The grey shadow areas denote time windows of bouncing events used for cross-correlation. (b) Aligned waveforms of three continuous bouncing events of sensor 16 at $cp = 30$ MPa and $ds = 10$ MPa.

The time interval between the $(k + 1)$ th and the k th bounce is then

$$\tilde{t}_{k+1}^j - \tilde{t}_k^j = \frac{2v_k}{g} = \frac{2a^k v_0}{g}, \quad (3)$$

where g is the acceleration of gravity. The theoretical bouncing time intervals $\delta t^j = [\tilde{t}_2^j - \tilde{t}_1^j, \dots, \tilde{t}_n^j - \tilde{t}_{n-1}^j]$ can then be modelled as

$$\delta t_m^j = \left[\frac{2av_0}{g}, \frac{2a^2v_0}{g}, \dots, \frac{2a^{n-1}v_0}{g} \right] \quad (4)$$

Now, modelling the mismatch between the modelled and measured time intervals with additive noise e_m^j , the bouncing time interval data δt^j is represented as

$$\delta t^j = \delta t_m^j + e_m^j. \quad (5)$$

The waveform recorded at receiver j due to the k th ball bounce, $\sigma^{j,k}(t)$, can be written as

$$\sigma^{j,k}(t) = L[I[u^{j,k}(\mathbf{r}^j, t)]] = L[I[f_k(t) * \mathbf{G}(\mathbf{r}^j, t)]], \quad (6)$$

where $u^{j,k}(\mathbf{r}^j, t)$ is the input displacement at receiver j due to the k th bounce of the ball, $f_k(t)$ is the loading function of the k th bounce of the ball, $\mathbf{G}(\mathbf{r}^j, t)$ is the Green's function representing the impulse response of the sample at receiver j , t is the time, \mathbf{r}^j is the vector directed from the bouncing ball source to receiver j , I is the incident angle correction, and L is a linear operator, assuming that the response function of the PZT transducer can be modelled as a linear time-invariant (LTI) system. Based on previous studies of ball collisions (McLaskey & Glaser 2012; McLaskey *et al.* 2015),

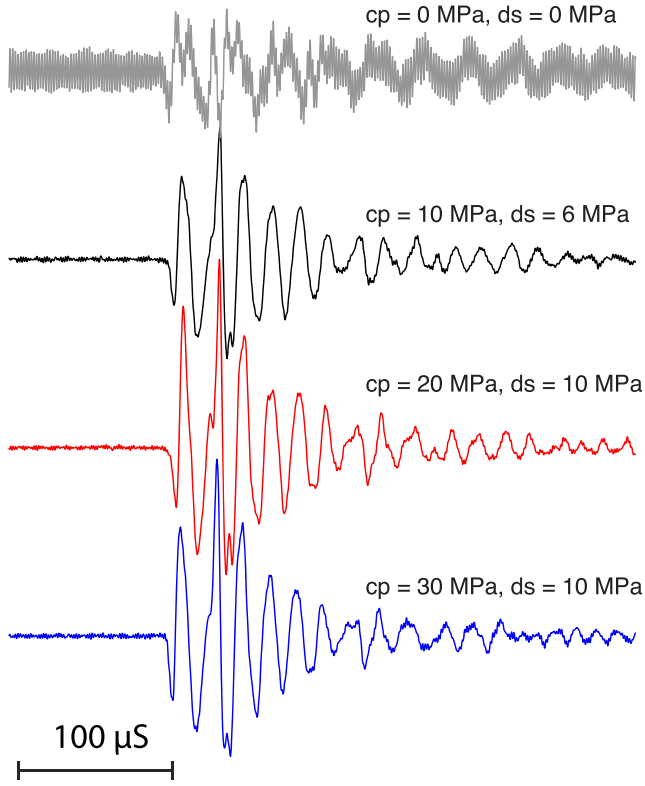


Figure 4. Waveforms at sensor 16 due to the first bounce of the ball drop at: (1) $cp = 10$ MPa, $ds = 6$ MPa; (2) $cp = 20$ MPa, $ds = 10$ MPa; (3) $cp = 30$ MPa, $ds = 10$ MPa; and (4) $cp = 0$ MPa, $ds = 0$ MPa. The waveforms are normalized by the maximum amplitudes of all waveforms.

the loading function can be represented as

$$f_k(t) = -F_{\max,k} \sin\left(\frac{\pi t}{t_c}\right)^{3/2}, \quad 0 \leq |t| \leq t_c, \quad (7)$$

$$f_k(t) = 0, \quad \text{otherwise,}$$

where $F_{\max,k}$ is the maximum loading force of the k th ball bounce and t_c is the total loading time, which is the entire contact time between the ball and the top surface of the sample. The $F_{\max,k}$ and t_c are modelled as

$$F_{\max,k} = 1.917 \rho_1^{3/5} (\delta_1 + \delta_2)^{-2/5} R_1^2 v_{k-1}^{6/5}, \quad (8)$$

$$\delta_q = \frac{1 - \mu_q^2}{\pi E_q}, \quad q = 1, 2 \quad (9)$$

$$t_c = 1/f_c = 4.53(4\rho_1\pi(\delta_1 + \delta_2)/3)^{2/5} R_1 v_{k-1}^{-1/5}, \quad (10)$$

where ρ_q , E_q , μ_q are the density, Young's modulus, and Poisson's ratio of the q th material, respectively ($q = 1$ refers to the steel ball and $q = 2$ refers to the titanium sample). In this experiment, $\rho_1 = 8050 \text{ kg m}^{-3}$, $E_1 = 180.0 \text{ GPa}$, $\mu_1 = 0.305$, $\rho_2 = 4506 \text{ kg m}^{-3}$, $E_2 = 113.8 \text{ GPa}$ and $\mu_2 = 0.32$. v_{k-1} is the incident velocity of the k th bounce of the ball.

$G_{i3}(\mathbf{r}^j, t)$ is the i th ($i = 1, 2, 3$, corresponding to three axes) component of displacement at a generic (\mathbf{r}^j, t) , for an impulsive point force source in the x_3 direction, that is, the vertical direction. The i th component of displacement due to the k th bounce, $u_i^{j,k}(\mathbf{r}^j, t)$, is

represented as (Aki & Richards 2002)

$$u_i^{j,k}(\mathbf{r}^j, t) = f_k(t) * G_{i3}(\mathbf{r}^j, t),$$

$$= \frac{1}{4\pi\rho_2} (3\gamma_i^j \gamma_3^j - \delta_{i3}) \frac{1}{(r^j)^3} \int_{r^j/V_P}^{r^j/V_S} \tau f_k(t - \tau) d\tau$$

$$+ \frac{1}{4\pi\rho_2 V_P^2} \gamma_i^j \gamma_3^j \frac{1}{r^j} f_k\left(t - \frac{r^j}{V_P}\right)$$

$$- \frac{1}{4\pi\rho_2 V_S^2} (\gamma_i^j \gamma_3^j - \delta_{i3}) \frac{1}{r^j} f_k\left(t - \frac{r^j}{V_S}\right), \quad (11)$$

where $V_P = 6011.6 \text{ m s}^{-1}$ and $V_S = 3093.0 \text{ m s}^{-1}$ are the P - and S -wave velocity of the titanium sample, respectively; r^j is the norm of the vector from the source to sensor j ; γ_i^j is the directional cosine between this vector and the i th coordinate axis; and δ_{i3} is the Kronecker delta. This Green's function is for a homogeneous, isotropic, unbounded medium. We use this approximation because we do not observe coherent signals due to possible reflections from boundaries in the data. Secondly, the finite difference modelling in Appendix C shows that for our calibration system with a Titanium sample, this homogeneous, isotropic, unbounded medium approximation produces almost identical waveforms compared to the system with a Titanium–Steel boundary on the top. The ball drop apparatus is made of Steel.

The incidence angle dependence of the sensor is assumed to be a cosine function, that is,

$$I[u^{j,k}(\mathbf{r}^j, t)] = u_{\perp}^{j,k}(\mathbf{r}^j, t) = \sum_{i=1}^3 u_i^{j,k}(\mathbf{r}^j, t) \xi_i^j, \quad (12)$$

where ξ_i^j is the directional cosine of the normal vector of sensor j , that is, $[r_1^j, r_2^j, 0]$. This cosine approximation is justified in Appendix B.

The frequency response function of sensor j is modelled by

$$\mathfrak{R}^j(\omega) = \frac{-C\omega^2}{\omega^2 + 2i\varepsilon^j\omega - (\omega_s^j)^2}, \quad (13)$$

where ω_s^j is the resonance frequency, ε^j is the damping coefficient of sensor j and C is the conversion constant with units count m^{-1} . This simple frequency response function of a damped oscillator can fully describe the resonance and damping effects of PZT sensors according to the full waveform matching, so we do not include high-fidelity PZT sensor modelling method in our model (Bæk *et al.* 2010). Eq. (13) has also been used to model the frequency-response of an inertial seismometer (Aki & Richards 2002).

Then the noise-free signal at sensor j due to the k th bounce can be represented as

$$O^{j,k}(\omega) = \mathfrak{R}^j(\omega) U_{\perp}^{j,k}(\omega) \quad (14)$$

in the frequency domain, and

$$o^{j,k}(t) = \tau^j(t) * u_{\perp}^{j,k}(t) \quad (15)$$

in the time domain, where $*$ represents the convolution operator. In (14), $U_{\perp}^{j,k}(\omega)$ is simply the Fourier transform of $u_{\perp}^{j,k}(t)$ (12). Similarly, $\tau^j(t)$ is the inverse Fourier transform of $\mathfrak{R}^j(\omega)$ (13). Concatenating waveforms from all the bounces, along with their corresponding noise perturbations $\phi^{j,k}(t)$, the data at receiver j can

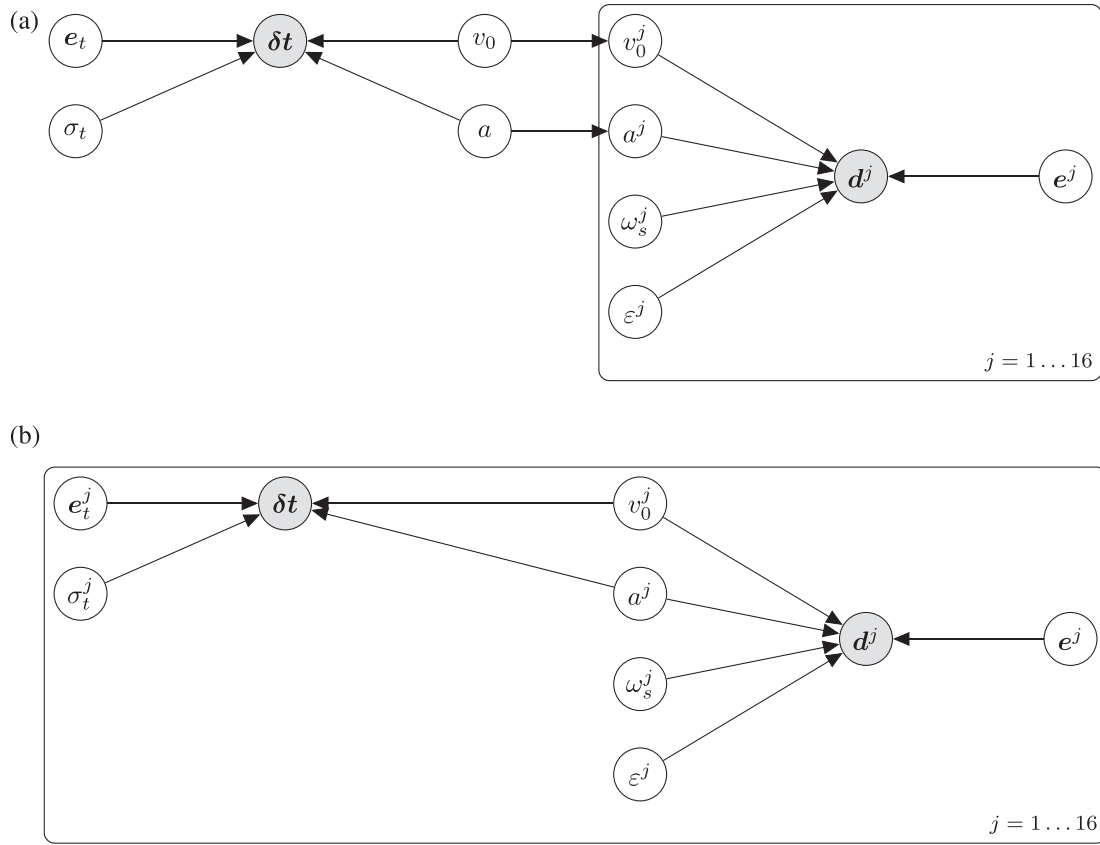


Figure 5. Schematic of MCMC procedure. (a) The hierarchical model; (b) the decoupled model.

Table 1. Posterior mean and standard deviation (SD) of $(\sigma_t^j)^2$, v_0^j , a^j , ω_s^j and ϵ^j for 16 sensors at $cp = 10$ MPa and $ds = 6$ MPa.

ID	α^j	$(\sigma_t^j)^2$ ($10^{-10} s^2$)		v_0^j ($m s^{-1}$)		a^j		ω_s^j (kHz)		ϵ^j (kHz)	
		Mean	SD	Mean	SD	Mean	SD	Mean	SD	Mean	SD
1	0.144	0.918	0.074	1.02E+00	4.82E-05	6.74E-01	2.29E-05	341.63	0.19	17.44	0.12
2	0.027	0.918	0.074	1.02E+00	4.79E-05	6.74E-01	2.28E-05	321.97	0.05	19.55	0.05
3	0.007	0.919	0.075	1.02E+00	4.80E-05	6.74E-01	2.28E-05	327.47	0.01	10.88	0.02
4	0.019	0.915	0.073	1.02E+00	4.81E-05	6.74E-01	2.28E-05	362.52	0.05	17.66	0.04
5	0.128	0.918	0.074	1.02E+00	4.79E-05	6.74E-01	2.28E-05	339.19	0.27	23.63	0.18
6	0.059	0.918	0.074	1.02E+00	4.80E-05	6.74E-01	2.29E-05	316.82	0.15	37.85	0.17
7	0.012	0.916	0.074	1.02E+00	4.78E-05	6.74E-01	2.27E-05	338.36	0.03	15.83	0.03
8	0.019	0.917	0.074	1.02E+00	4.77E-05	6.74E-01	2.27E-05	354.41	0.08	35.49	0.10
9	0.137	0.918	0.074	1.02E+00	4.79E-05	6.74E-01	2.28E-05	332.08	0.18	16.80	0.16
10	0.015	0.918	0.074	1.02E+00	4.80E-05	6.74E-01	2.28E-05	327.44	0.03	15.03	0.03
11	0.028	0.918	0.074	1.02E+00	4.82E-05	6.74E-01	2.30E-05	315.49	0.10	43.12	0.14
12	0.025	0.917	0.074	1.02E+00	4.78E-05	6.74E-01	2.28E-05	343.71	0.09	29.54	0.09
13	–	–	–	–	–	–	–	–	–	–	–
14	0.044	0.918	0.074	1.02E+00	4.81E-05	6.74E-01	2.29E-05	310.41	0.07	23.17	0.08
15	0.023	0.918	0.075	1.02E+00	4.81E-05	6.74E-01	2.30E-05	337.57	0.08	34.43	0.10
16	0.006	0.922	0.073	1.02E+00	4.87E-05	6.74E-01	2.35E-05	348.49	0.02	14.93	0.02

Table 2. Posterior mean and standard deviation (*SD*) of $(\sigma_t^j)^2$, v_0^j , a^j , ω_s^j and ε^j for 16 sensors at $cp = 20$ MPa and $ds = 10$ MPa.

ID	α^j	$(\sigma_t^j)^2$ ($10^{-10}s^2$)		v_0^j ($m\ s^{-1}$)		a^j		ω_s^j (kHz)		ε^j (kHz)	
		Mean	<i>SD</i>	Mean	<i>SD</i>	Mean	<i>SD</i>	Mean	<i>SD</i>	Mean	<i>SD</i>
1	0.082	0.918	0.074	1.13E+00	4.89E-05	6.64E-01	2.08E-05	343.14	0.29	21.87	0.12
2	0.011	0.917	0.074	1.13E+00	4.90E-05	6.64E-01	2.09E-05	337.33	0.04	18.80	0.03
3	0.007	0.918	0.074	1.13E+00	4.88E-05	6.63E-01	2.08E-05	332.10	0.02	18.01	0.03
4	0.010	0.917	0.074	1.13E+00	4.92E-05	6.64E-01	2.08E-05	354.77	0.04	24.08	0.04
5	0.070	0.918	0.074	1.13E+00	4.91E-05	6.64E-01	2.08E-05	339.54	0.18	27.82	0.16
6	0.026	0.918	0.075	1.13E+00	4.89E-05	6.64E-01	2.08E-05	315.00	0.09	35.76	0.11
7	0.006	0.918	0.074	1.13E+00	4.92E-05	6.64E-01	2.09E-05	334.67	0.02	16.98	0.02
8	0.012	0.918	0.074	1.13E+00	4.89E-05	6.64E-01	2.08E-05	335.91	0.07	42.97	0.08
9	0.061	0.918	0.074	1.13E+00	4.88E-05	6.64E-01	2.08E-05	341.97	0.19	15.30	0.13
10	0.010	0.917	0.074	1.13E+00	4.93E-05	6.63E-01	2.09E-05	340.14	0.04	17.14	0.03
11	0.026	0.918	0.075	1.13E+00	4.92E-05	6.64E-01	2.09E-05	338.87	0.11	39.78	0.13
12	0.011	0.918	0.074	1.13E+00	4.91E-05	6.64E-01	2.08E-05	341.11	0.06	31.49	0.07
13	–	–	–	–	–	–	–	–	–	–	–
14	0.029	0.917	0.074	1.13E+00	4.94E-05	6.64E-01	2.09E-05	320.88	0.06	20.32	0.06
15	0.011	0.918	0.074	1.13E+00	4.89E-05	6.64E-01	2.07E-05	340.89	0.05	31.11	0.06
16	0.003	0.917	0.073	1.13E+00	4.93E-05	6.64E-01	2.08E-05	350.82	0.01	16.76	0.01

Table 3. Posterior mean and standard deviation (*SD*) of $(\sigma_t^j)^2$, v_0^j , a^j , ω_s^j and ε^j for 16 sensors at $cp = 30$ MPa and $ds = 10$ MPa.

ID	α^j	$(\sigma_t^j)^2$ ($10^{-10}s^2$)		v_0^j ($m\ s^{-1}$)		a^j		ω_s^j (kHz)		ε^j (kHz)	
		Mean	<i>SD</i>	Mean	<i>SD</i>	Mean	<i>SD</i>	Mean	<i>SD</i>	Mean	<i>SD</i>
1	0.103	0.917	0.074	1.31100	5.42E-05	0.61152	1.88E-05	321.48	0.15	12.93	0.11
2	0.013	0.918	0.074	1.31115	5.42E-05	0.61147	1.87E-05	330.47	0.03	18.26	0.03
3	0.005	0.917	0.074	1.31130	5.47E-05	0.61144	1.89E-05	338.42	0.02	22.00	0.03
4	0.012	0.916	0.074	1.31102	5.48E-05	0.61152	1.90E-05	364.67	0.04	22.77	0.04
5	0.074	0.917	0.074	1.31103	5.44E-05	0.61151	1.89E-05	323.93	0.17	34.76	0.17
6	0.030	0.918	0.074	1.31104	5.46E-05	0.61151	1.90E-05	311.61	0.08	31.06	0.10
7	0.006	0.918	0.075	1.31122	5.53E-05	0.61146	1.91E-05	339.36	0.02	15.50	0.02
8	0.014	0.918	0.074	1.31102	5.45E-05	0.61152	1.89E-05	356.53	0.08	40.51	0.09
9	0.085	0.918	0.074	1.31103	5.48E-05	0.61151	1.90E-05	333.22	0.11	23.96	0.14
10	0.012	0.918	0.074	1.31128	5.44E-05	0.61143	1.88E-05	335.74	0.03	17.36	0.03
11	0.016	0.918	0.074	1.31111	5.45E-05	0.61149	1.89E-05	347.06	0.07	34.66	0.08
12	0.013	0.917	0.074	1.31116	5.47E-05	0.61147	1.90E-05	347.68	0.06	26.62	0.06
13	–	–	–	–	–	–	–	–	–	–	–
14	0.021	0.919	0.074	1.31110	5.49E-05	0.61149	1.91E-05	319.47	0.05	19.52	0.05
15	0.012	0.918	0.074	1.31101	5.43E-05	0.61152	1.88E-05	335.04	0.05	30.65	0.05
16	0.004	0.917	0.073	1.31064	5.46E-05	0.61167	1.87E-05	358.74	0.01	17.55	0.02

be modelled as

$$\begin{bmatrix} d^{j,1}(t) \\ d^{j,2}(t) \\ \vdots \\ d^{j,k}(t) \\ \vdots \\ d^{j,n}(t) \end{bmatrix} = \begin{bmatrix} o^{j,1}(t) \\ o^{j,2}(t) \\ \vdots \\ o^{j,k}(t) \\ \vdots \\ o^{j,n}(t) \end{bmatrix} + \begin{bmatrix} e^{j,1}(t) \\ e^{j,2}(t) \\ \vdots \\ e^{j,k}(t) \\ \vdots \\ e^{j,n}(t) \end{bmatrix}, \quad (16)$$

which can be written more compactly as

$$d^j(t) = o^j(t) + e^j(t), \quad (17)$$

and, after time discretization, as

$$d^j = o^j + e^j. \quad (18)$$

2.3 Bayesian formulation and posterior sampling

In principle, one could use a Bayesian hierarchical model to represent the entire ball drop system, given bouncing time interval data $\delta t := \{\delta t^j\}_{j=1}^{16}$ and waveform data $\{d^j\}_{j=1}^{16}$ from all 16 sensors. The resulting posterior density is:

$$\begin{aligned} & P\left(\{v_0^j, a^j, \omega_s^j, \varepsilon^j\}_{j=1}^{16}, v_0, a, \sigma_t^2 | \{d^j\}_{j=1}^{16}, \delta t\right) \\ & \propto P(\delta t | v_0, a, \sigma_t^2) P(v_0) P(a) P(\sigma_t^2) \\ & \times \left(\prod_{j=1}^{16} P(d^j | v_0^j, a^j, \omega_s^j, \varepsilon^j) \right) \left(\prod_{j=1}^{16} P(v_0^j, a^j | v_0, a) \right) \\ & \times \left(\prod_{j=1}^{16} P(v_0^j) P(a^j) P(\omega_s^j) P(\varepsilon^j) \right), \quad (19) \end{aligned}$$

We explain this model, and the terms above, as follows. First, there is in principle a single true value of the ball's initial incident velocity and rebound coefficient, represented by the 'master' parameters v_0

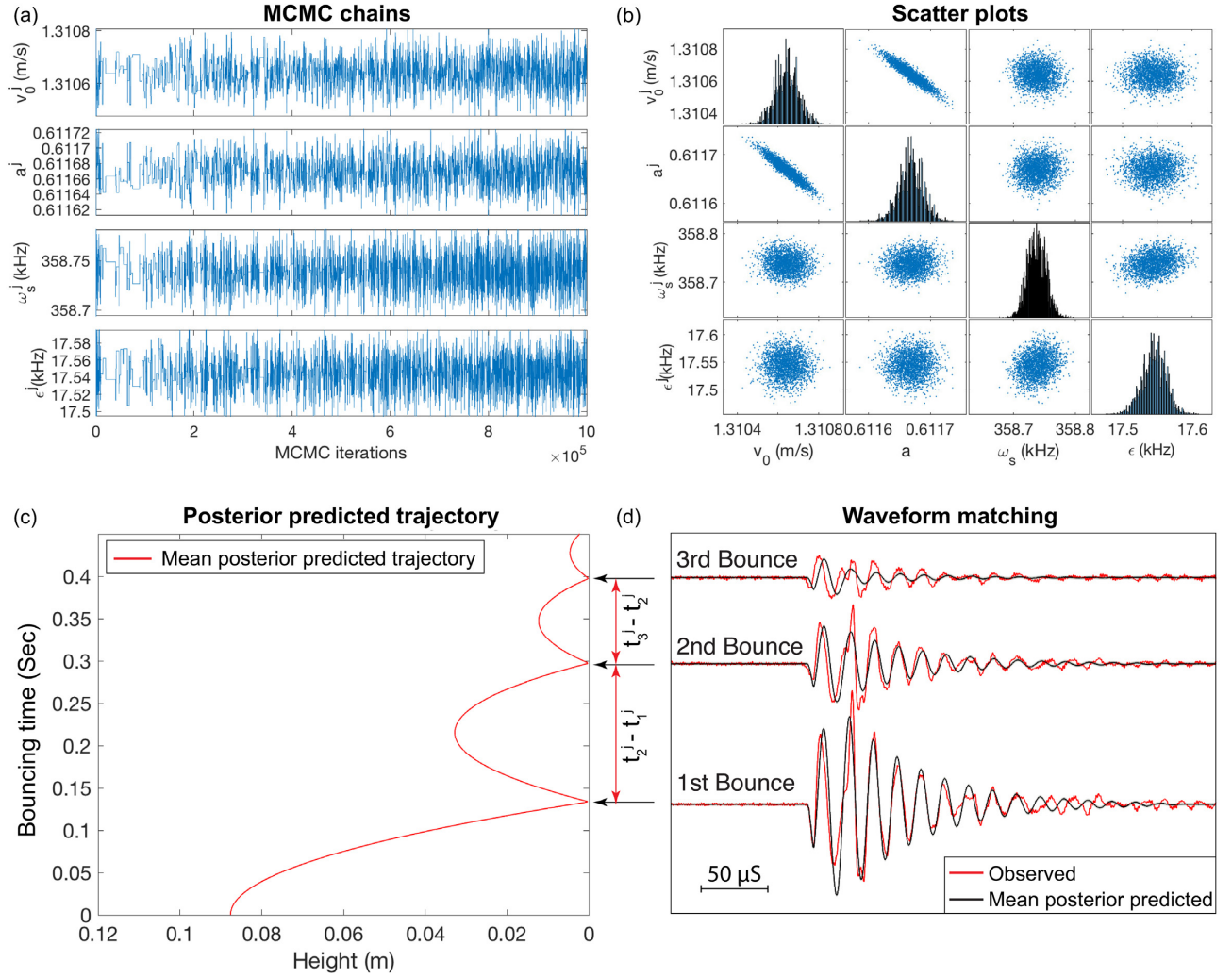


Figure 6. MCMC chains and posterior distribution of four parameters for sensor 16. The first 6×10^5 iterations of MCMC chains are discarded as burn-in. (a) MCMC chains for initial velocity v_0^j , rebound coefficient a^j , resonance frequency ω_s^j , and damping coefficient ϵ^j . (b) Scatter plots of four parameters corresponding to MCMC chains. (c) Mean posterior predicted trajectory of ball bouncing. (d) Waveform comparison between observed (red) and mean posterior predicted waveforms (black).

and a . All of the bouncing time intervals δt should depend on these values; this relationship is encoded in the conditional probability density $P(\delta t | v_0, a, \sigma_t^2)$. Here σ_t^2 is the variance of the noise e_t^j in (5), which we also wish to infer. The full waveforms \mathbf{d}^j at each receiver j also depend on the ball velocity and rebound coefficient, however, as these are needed to determine the loading function for each individual bounce $k = 1, \dots, n$. Due to noise and unmodelled dynamics, these waveforms may be better represented by slightly different local bouncing parameters, v_0^j and a^j , at each receiver j . To relate the local bouncing parameters v_0^j and a^j with the master parameters v_0 and a , as is typical in Bayesian hierarchical modelling (Gelman *et al.* 2013), the model above uses the conditional distributions $P(v_0^j, a^j | v_0, a)$. The relationship between the local bouncing parameters and the full waveforms is encoded in the likelihood $P(\mathbf{d}^j | v_0^j, a^j, \omega_s^j, \epsilon^j)$.

To simplify and decouple this inference problem, however, we can ignore the relationship between the master (v_0, a) and (v_0^j, a^j) , that is, we can assume $P(v_0^j, a^j | v_0, a) \approx P(v_0^j, a^j)$. Then the master parameters become irrelevant and we can infer parameters $\mathbf{X} = [v_0^j, a^j, \omega_s^j, \epsilon^j]$ and a variance $(\sigma_t^j)^2$ for each sensor separately. This assumption is reasonable because there is a considerable amount of

data/information at each sensor; thus, there is little to be gained by ‘sharing strength’ via the common parameters (v_0, a) . For sensor j , the posterior probability density $P(v_0^j, a^j, \omega_s^j, \epsilon^j, (\sigma_t^j)^2 | \mathbf{d}^j, \delta t)$ is then written as

$$\begin{aligned}
 P(v_0^j, a^j, \omega_s^j, \epsilon^j, (\sigma_t^j)^2 | \mathbf{d}^j, \delta t) &\propto P(\delta t | v_0^j, a^j, (\sigma_t^j)^2) \\
 &\quad \times P(\mathbf{d}^j | v_0^j, a^j, \omega_s^j, \epsilon^j) \\
 &\quad \times P(v_0^j)P(a^j) \\
 &\quad \times P(\omega_s^j)P(\epsilon^j)P((\sigma_t^j)^2). \quad (20)
 \end{aligned}$$

Fig. 5 represents the hierarchical Bayesian model and the simplified Bayesian model graphically, as Bayesian networks.

Now we define the specific prior and likelihood terms in the posterior probability density function (20). We use uniform prior distributions for v_0^j, a^j, ω_s^j , and ϵ^j , that is,

$$\begin{aligned}
 v_0^j &\sim \mathcal{U}(1.0, 1.5) \text{ m/s}, & a^j &\sim \mathcal{U}(0.5, 0.9), \\
 \omega_s^j &\sim \mathcal{U}(100, 500) \text{ kHz}, & \epsilon^j &\sim \mathcal{U}(10, 50) \text{ kHz},
 \end{aligned} \quad (21)$$

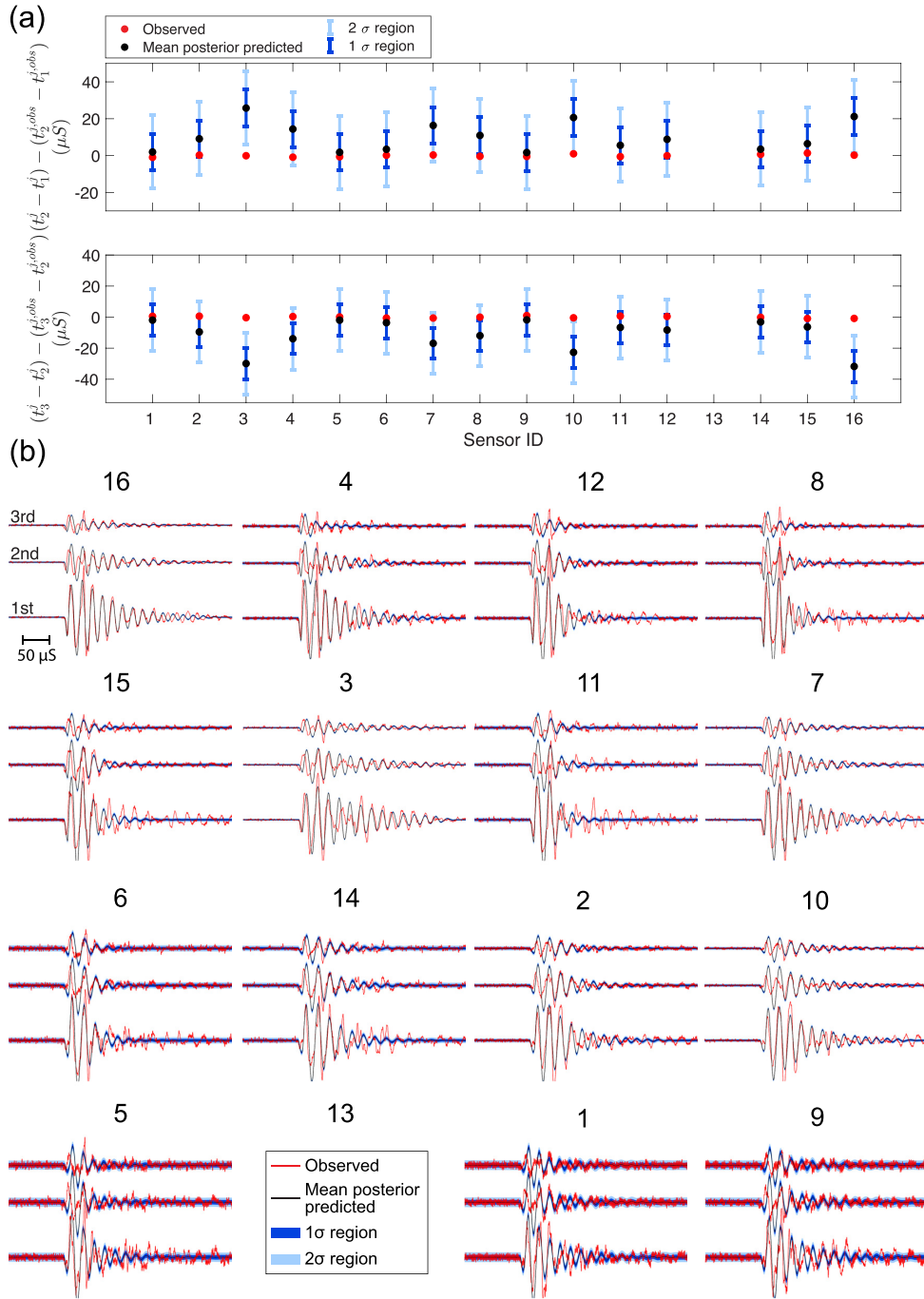


Figure 7. Results at $cp = 10$ MPa, $ds = 6$ MPa: (a) Comparison between observed (red) and mean posterior predicted (blue) bouncing time intervals. The error bars indicate the 1σ and 2σ regions. (b) Waveform comparison between observed (red) and mean posterior predicted (black) waveforms of three bouncing events for 16 PZT sensors. Blue and light blue shading areas show the 1σ and 2σ regions of posterior predicted waveforms after the burn-in. The title of each subplot denotes sensor ID. Subplots are arranged in the order of sensor locations shown in Fig. 2. Sensor 13 did not work, so we put the legend in the position of sensor 13.

and a normal distribution for $(\sigma_t^j)^2$,

$$(\sigma_t^j)^2 \sim \mathcal{N}(10^{-10}, 10^{-22}) s^2. \quad (22)$$

The likelihood functions $P(\delta \mathbf{t} | v_0^j, a^j)$ and $P(\mathbf{d}^j | v_0^j, a^j, \omega_s^j, \varepsilon^j)$ depend on the probability distributions of $\mathbf{e}_t = \delta \mathbf{t} - \delta \mathbf{t}_m$ (5) and $\mathbf{e}^j = \mathbf{d}^j - \mathbf{o}^j$ (17), respectively. In this paper, we assume that both

errors are Gaussian, with zero mean and diagonal covariance matrices Σ_t and Σ^j , respectively. The diagonal entries of Σ_t are

$$\Sigma_{t,ii} = (\sigma_t^j)^2, \quad i = 1, 2, \dots, N_{\delta t}, \quad (23)$$

where $N_{\delta t}$ is the total number of bouncing time intervals, collected over all the sensors. The diagonal entries of Σ^j are

$$\Sigma_{ii}^j = (\sigma^j)^2, \quad i = 1, 2, \dots, N, \quad (24)$$

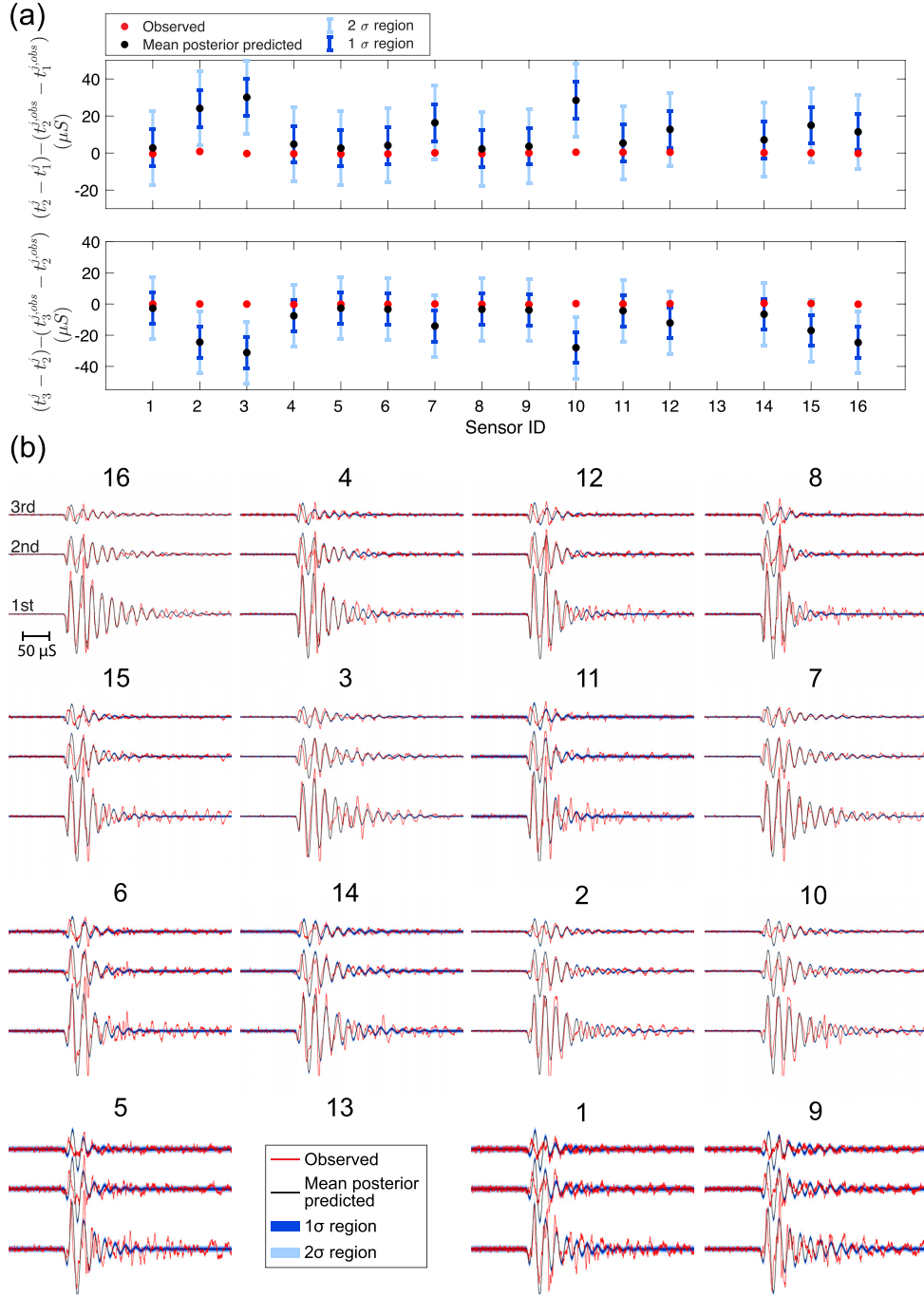


Figure 8. Results at $cp = 20$ MPa, $ds = 10$ MPa: (a) Comparison between observed (red) and mean posterior predicted (blue) bouncing time intervals. The error bars indicate the 1σ and 2σ regions. (b) Waveform comparison between observed (red) and mean posterior predicted (black) waveforms of three bouncing events for 16 PZT sensors. Blue and light blue shading areas show the 1σ and 2σ regions of posterior predicted waveforms after the burn-in. The title of each subplot denotes sensor ID. Subplots are arranged in the order of sensor locations shown in Fig. 2. Sensor 13 did not work, so we put the legend in the position of sensor 13.

where N is the total number of data samples (time discretization points) for the waveforms \mathbf{d}^j . Then the likelihood functions can be written as

$$P(\delta\mathbf{t}|v_0^j, \mathbf{a}^j, (\sigma_t^j)^2) = \frac{1}{\sqrt{(2\pi)^{N_{dt}} \det \Sigma_t}} \times \exp\left[-\frac{1}{2}(\delta\mathbf{t} - \delta\mathbf{t}_m)^T \Sigma_t^{-1}(\delta\mathbf{t} - \delta\mathbf{t}_m)\right], \quad (25)$$

$$P(\mathbf{d}^j|v_0^j, \mathbf{a}^j, \omega_s^j, \varepsilon^j) = \frac{1}{\sqrt{(2\pi)^N \det \Sigma^j}} \times \exp\left[-\frac{1}{2}(\mathbf{d}^j - \mathbf{o}^j)^T (\Sigma^j)^{-1}(\mathbf{d}^j - \mathbf{o}^j)\right]. \quad (26)$$

The variance parameter $(\sigma_t^j)^2$ represents a trade-off between the influence of the bouncing time interval data and the waveform data. As encoded in the posterior distribution (20), it is inferred from both sets of data, for each sensor j . The variance parameter $(\sigma^j)^2$,

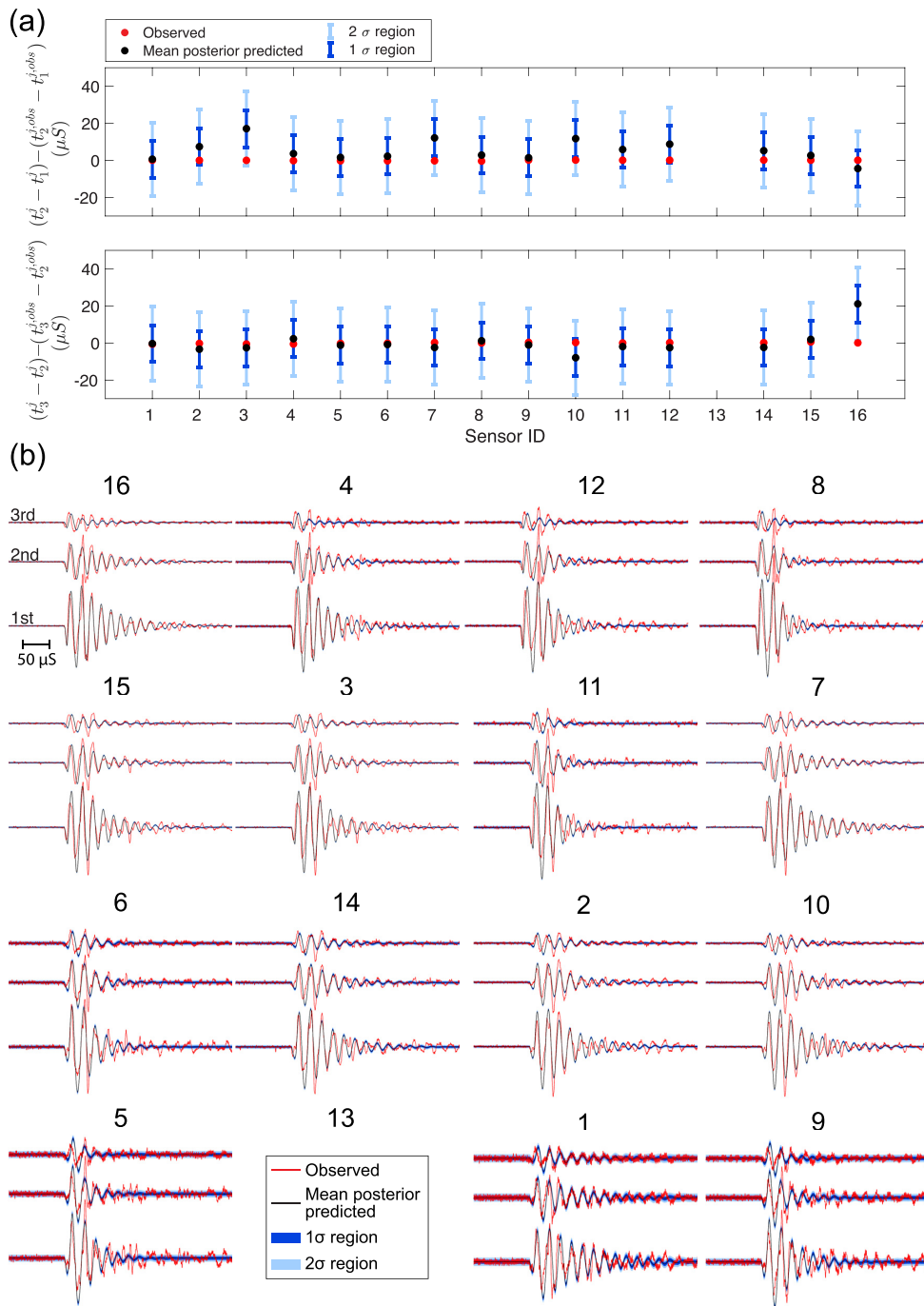


Figure 9. Results at $cp = 30$ MPa, $ds = 10$ MPa: (a) Comparison between observed (red) and mean posterior predicted (blue) bouncing time intervals. The error bars indicate the 1σ and 2σ regions. (b) Waveform comparison between observed (red) and mean posterior predicted (black) waveforms of three bouncing events for 16 PZT sensors. Blue and light blue shading areas show the 1σ and 2σ regions of posterior predicted waveforms after the burn-in. The title of each subplot denotes sensor ID. Subplots are arranged in the order of sensor locations shown in Fig. 2. Sensor 13 did not work, so we put the legend in the position of sensor 13.

on the other hand, is not inferred within the Bayesian model, but is determined based on the noise level of the waveform data. In particular, we set it to be a fraction $\alpha^j \in (0, 1)$ of the power of the waveform data d^j , that is,

$$\begin{aligned} (\sigma^j)^2 &= \alpha^j \frac{1}{T} \int_0^T (d^j(t))^2 dt \approx \alpha^j \frac{1}{T} \sum_{i=1}^N \Delta t (d_i^j)^2 \\ &= \alpha^j \frac{1}{N} \sum_{i=1}^N (d_i^j)^2, \end{aligned} \quad (27)$$

where T is the total time length of waveform data, $N = T/\Delta t$ is the number of time discretization points and $d_i^j = d^j(t_i)$. We estimate α^j , the ratio of noise and waveform data power for sensor j , as

$$\alpha^j = \frac{\frac{1}{T_b} \int_0^{T_b} b^2(t) dt}{\frac{1}{T} \int_0^T d^2(t) dt} \approx \frac{\frac{1}{T_b} \sum_{i=1}^{N_b} \Delta t (b_i^j)^2}{\frac{1}{T} \sum_{i=1}^N \Delta t (d_i^j)^2} = \frac{N \sum_{i=1}^{N_b} (b_i^j)^2}{N_b \sum_{i=1}^N (d_i^j)^2}, \quad (28)$$

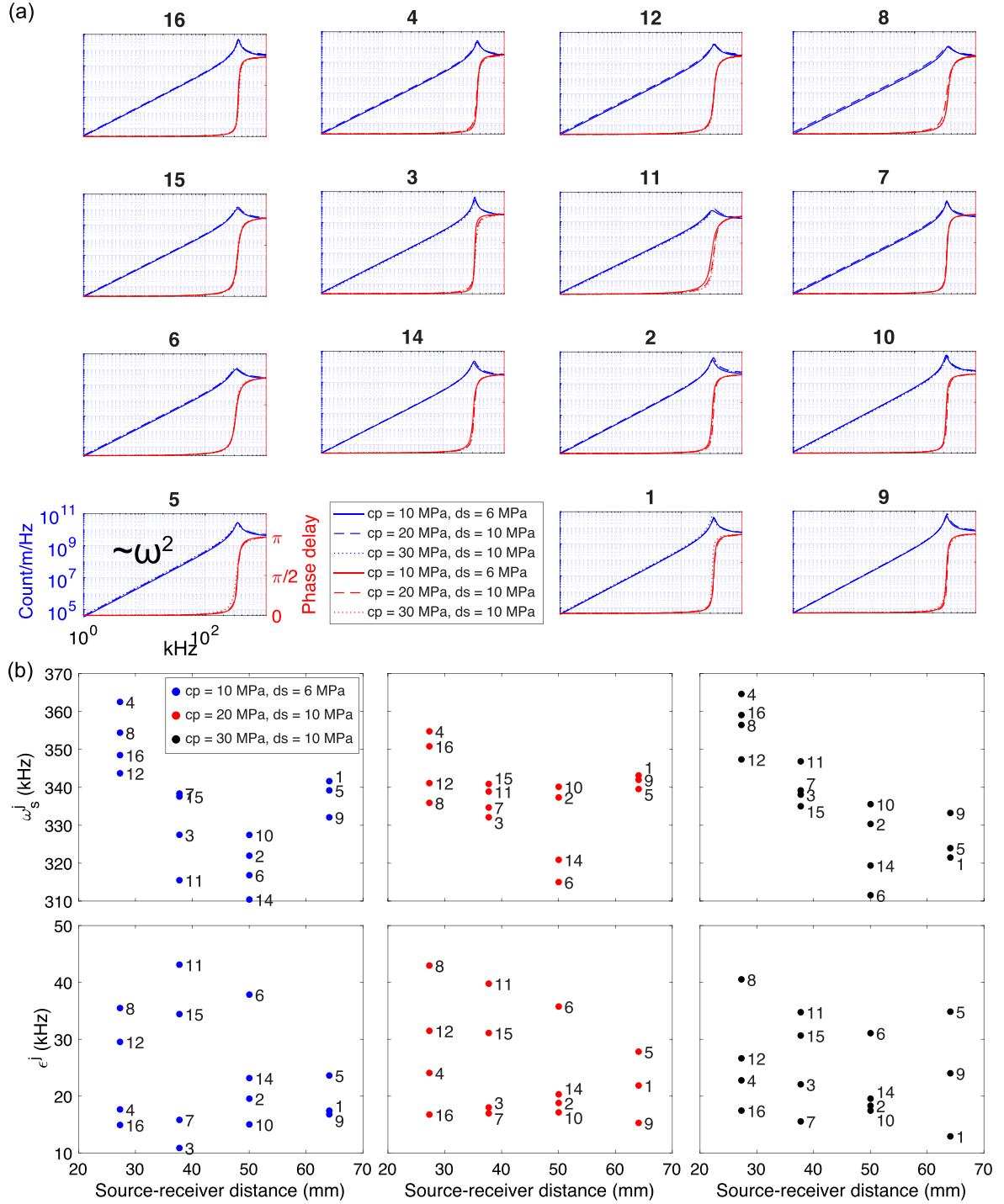


Figure 10. Transfer functions at different cp and ds. (a) Mean posterior predicted amplitude response (blue) and phase delay (red). The amplitude response tends to a constant at high frequencies, and is proportional to ω^2 at low frequencies. The title of each subplot denotes sensor ID. Subplots are arranged in the order of sensor locations shown in Fig. 2. Sensor 13 did not work, so we put the legend in the position of sensor 13. (b) ω_s^j and ϵ^j as a function of source–receiver distance.

where $b(t)$ is the recorded noise before the first P arrival of the first bouncing event, T_b is the time length of the noise window and $N_b = T_b/\Delta t$ is the number of noise samples. Substituting (28) into (27), we obtain

$$(\sigma^j)^2 = \frac{1}{N_b} \sum_{i=1}^{N_b} (b_i^j)^2. \quad (29)$$

For each sensor j , we use Markov chain Monte Carlo (MCMC) sampling to characterize the posterior distribution given by (20). We use an independence proposal from the prior to update $(\sigma_i^j)^2$ and a Gaussian random-walk proposal with adaptive covariance to update \mathbf{X} . The 5-D vector of proposed values for $(\mathbf{X}, (\sigma_i^j)^2)$ is then accepted or rejected according to the standard Metropolis-Hastings criterion (Metropolis *et al.* 1953; Hastings 1970). The proposal for \mathbf{X} follows the adaptive Metropolis (AM) approach of Haario

et al. (2001), adjusting the proposal covariance matrix based on all previous samples of \mathbf{X} :

$$C_\ell^* = s_d \text{Cov}(\mathbf{X}_0, \dots, \mathbf{X}_\ell) + s_d \epsilon_0 I_d. \quad (30)$$

Here C_ℓ^* is the proposal covariance matrix at step ℓ , I_d is the d -dimensional identity matrix, $\epsilon_0 > 0$ is a small constant to make C_ℓ^* positive definite, $d = 4$ is the dimension of \mathbf{X} , and $s_d = 2.4^2/d$. The value of the scaling parameter s_d is a standard choice to optimize the mixing properties of the Metropolis search (Gelman *et al.* 1996). This value might affect the efficiency of MCMC, but not the posterior distribution itself.

3 RESULTS AND DISCUSSION

We apply the Bayesian method to all 16 sensors at (1) cp = 10 MPa, ds = 6 MPa; (2) cp = 20 MPa, ds = 10 MPa and (3) cp = 30 MPa, ds = 10 MPa. (sensor 13 did not work during the experiment). For each sensor, we first calculate the parameter α^j using (28). The values of α^j for the 16 sensors are shown in Tables 1–3. The sensors at the top half of the cylinder sample (sensors 16, 4, 12, 8, 15, 3, 11, 7), which are closer to the ball bouncing source, generally have lower α^j than sensors at the bottom half of the cylinder sample, for example, sensors 6, 14, 2, 10, 5, 13, 1, 9. This is because the sensors close to the source have better signal-to-noise ratio than sensors away from the source; in other words, α^j is an indicator of signal quality.

We perform 10^6 MCMC iterations to explore the posterior (20) for each sensor at varied pressures. The first 6×10^5 iterations of each MCMC chain are discarded as burn-in. We show MCMC chains and posterior distributions of v_0^j , a^j , ω_s^j and ε^j for sensor 16 at cp = 30 MPa, ds = 10 MPa in Figs 6(a) and (b). Fig. 6(c) shows the mean posterior predicted trajectory of ball bouncing events. The comparison between the observed AE data and mean posterior predicted waveforms is shown in Fig. 6(d).

The marginal posterior distributions of $(\sigma_t^j)^2$, v_0^j , a^j , ω_s^j and ε^j at (1) cp = 10 MPa, ds = 6 MPa; (2) cp = 20 MPa, ds = 10 MPa and (3) cp = 30 MPa, ds = 10 MPa are summarized (via their means and standard deviations) in Tables 1–3. The parameters ω_s^j and ε^j for sensors closer to the bouncing source have higher posterior standard deviations than for sensors farther away from the bouncing source.

The posterior distributions of $(\sigma_t^j)^2$, v_0^j and a^j are relatively similar across the sensors; this is expected, as the bouncing time data sets are the same for all sensors. Note that the posterior variance of $(\sigma_t^j)^2$ is roughly half of the prior variance, and that the mean of $(\sigma_t^j)^2$ shifts slightly from its prior value.

Figs 7(a), 8(a) and 9(a) show the comparison between observed and mean posterior predicted bouncing time intervals, $t_2^j - t_1^j$ and $t_3^j - t_2^j$, for all the sensors at (1) cp = 10 MPa, ds = 6 MPa; (2) cp = 20 MPa, ds = 10 MPa and (3) cp = 30 MPa, ds = 10 MPa. The bias is smaller than 20 μs . Figs 7(b), 8(b) and 9(b) show the comparison between observed and mean posterior predicted waveforms. The observed waveforms are all well predicted. Blue and light blue shaded areas show the 1σ and 2σ regions of the posterior predictive waveforms (marginal intervals at each time step).

The 2σ region of the posterior predictive waveforms (light blue shadow areas) almost covers the observed waveforms. The higher the noise levels of the observations, the larger the light blue shadow areas. In contrast, the sensors with high signal quality generally show larger bias in bouncing time intervals. This is probably because of the tradeoff between the likelihood functions $P(\delta t | v_0^j, a^j)$ and $P(d^j | v_0^j, a^j, \omega_s^j, \varepsilon^j)$.

The mean posterior resonance frequency ω_s^j for all the sensors varies from 310 to 365 kHz, and the damping coefficient ε^j varies from 11 to 43 kHz. The posterior standard deviations for ω_s^j and ε^j are all within 1 kHz. With the posterior distributions of ω_s^j and ε^j , we can obtain frequency-response functions of all sensors using (13)(a). The standard deviation indicates how reliable the response function of each sensor is. We show the mean posterior amplitude response and phase delay of all response functions at varied cp and ds in Fig. 10(a). The amplitude response tends to a constant at high frequencies, and is proportional to ω^2 at low frequencies. The amplitude response at higher cp is larger than that at lower cp, but the difference is not obvious. The phase delay is close to zero at low frequencies and tends to π at high frequencies. The *in situ* response functions can be used to calibrate real AE data, that is, convert digital AE data into time series with physical units, for fracturing experiments in rocks under high pressure conditions.

We plot ω_s^j and ε^j as a function of source–receiver distance in Fig. 10(b). ω_s^j shows a clear trend of decay with the increasing source–receiver distance, indicating that attenuation effects, which are not included in our model, should be taken into account in (11) to avoid mapping sample Q into instrument response functions. ε^j does not show any distance-dependent properties.

4 CONCLUSION

We develop a Bayesian waveform-based method to calibrate PZT sensors of a newly designed *in situ* ball drop system in a sealed pressure vessel. Taking full waveforms due to ball bounces as input data, the Bayesian method successfully infers the model parameters v_0^j , a^j , ω_s^j and ε^j . Both the posterior distributions of *in situ* response functions of PZT sensors and the trajectories of ball bounces are recovered by this method.

With the *in situ* estimation of frequency-dependent sensor response functions, we are able to convert the AE waveforms' amplitude and phase to real physical parameters (e.g. displacements or accelerations) under high pressure conditions. The obtained uncertainties of response functions indicate the reliability of each sensor.

Our proposed method was tested on a titanium cylinder with a very homogeneous structure. For more complex (and realistic) cases, additional work needs to be performed. A good estimate of wave speeds is required, and, for example, attenuation in other rock types can be significant (Lockner *et al.* 1977; Winkler *et al.* 1979). As shown in Fig. 10(b), attenuation may be mapped into instrument response if not accounted for. We believe that using multiple bounces, as we have done here, will allow for a better constraint of the attenuation of the sample as well as for estimating wave speeds using relative arrival times and cross-correlation methods (Waldhauser & Ellsworth 2000; Zhang & Thurber 2003; Fuenzalida *et al.* 2013; Weemstra *et al.* 2013).

ACKNOWLEDGEMENTS

This research was supported by Total, Shell Global and MIT Earth Resources Laboratory.

REFERENCES

- Aki, K. & Richards, P.G., 2002. *Quantitative Seismology*, University Science Books.
- Bæk, D., Jensen, J.A. & Willatzen, M., 2010. Modeling transducer impulse responses for predicting calibrated pressure pulses with the ultrasound simulation program field II, *J. acoust. Soc. Am.*, **127**(5), 2825–2835.

- Brantut, N., 2018. Time-resolved tomography using acoustic emissions in the laboratory, and application to sandstone compaction, *Geophys. J. Int.*, **213**(3), 2177–2192.
- Chen, Y.-H., Chew, W.C. & Liu, Q.-H., 1998. A three-dimensional finite difference code for the modeling of sonic logging tools, *J. acoust. Soc. Am.*, **103**(2), 702–712.
- Drouillard, T., 1987. Introduction to acoustic emission technology, in *Non-destructive Testing Handbook*, Vol. 5, The American Society for Non-destructive Testing.
- Drouillard, T., 1996. A history of acoustic emission, *J. acoust. Emission*, **14**(1), 1–34.
- Earle, P.S. & Shearer, P.M., 1994. Characterization of global seismograms using an automatic-picking algorithm, *Bull. seism. Soc. Am.*, **84**(2), 366–376.
- Fu, W., Ames, B., Bungler, A., Savitski, A. *et al.*, 2015. An experimental study on interaction between hydraulic fractures and partially-cemented natural fractures, in *Proceedings of the 49th US Rock Mechanics/Geomechanics Symposium*, American Rock Mechanics Association.
- Fuenzalida, A., Schurr, B., Lancieri, M., Sobiesiak, M. & Madariaga, R., 2013. High-resolution relocation and mechanism of aftershocks of the 2007 Tocopilla (Chile) earthquake, *Geophys. J. Int.*, **194**(2), 1216–1228.
- Gelman, A., Roberts, G.O., Gilks, W.R. *et al.*, 1996. Efficient metropolis jumping rules, *Bayesian Stat.*, **5**(599–608), 42.
- Gelman, A., Stern, H.S., Carlin, J.B., Dunson, D.B., Vehtari, A. & Rubin, D.B., 2013. *Bayesian Data Analysis*, Chapman and Hall/CRC.
- Goebel, T., Schorlemmer, D., Becker, T., Dresen, G. & Sammis, C., 2013. Acoustic emissions document stress changes over many seismic cycles in stick-slip experiments, *Geophys. Res. Lett.*, **40**(10), 2049–2054.
- Goodfellow, S., Nasser, M., Maxwell, S. & Young, R., 2015. Hydraulic fracture energy budget: Insights from the laboratory, *Geophys. Res. Lett.*, **42**(9), 3179–3187.
- Graham, C., Stanchits, S., Main, I. & Dresen, G., 2010. Comparison of polarity and moment tensor inversion methods for source analysis of acoustic emission data, *Int. J. Rock Mech. Min. Sci.*, **47**(1), 161–169.
- Grosse, C.U. & Ohtsu, M., 2008. *Acoustic Emission Testing*, Springer Science & Business Media.
- Haario, H., Saksman, E. & Tamminen, J., 2001. An adaptive metropolis algorithm, *Bernoulli*, **7**(2), 223–242.
- Hampton, J., Matzar, L., Hu, D., Gutierrez, M. *et al.*, 2015. Fracture dimension investigation of laboratory hydraulic fracture interaction with natural discontinuity using acoustic emission, in *Proceedings of the 49th US Rock Mechanics/Geomechanics Symposium*, American Rock Mechanics Association.
- Hastings, W.K., 1970. Monte Carlo sampling methods using Markov chains and their applications, *Biometrika*, **57**(1), 97–109.
- Kaiser, E., 1950. A study of acoustic phenomena in tensile test, *Dr.-Ing. dissertation*. Technical University of Munich.
- Kurz, J.H., Grosse, C.U. & Reinhardt, H.-W., 2005. Strategies for reliable automatic onset time picking of acoustic emissions and of ultrasound signals in concrete, *Ultrasonics*, **43**(7), 538–546.
- Kwiatak, G., Charalampidou, E.-M., Dresen, G. & Stanchits, S., 2014a. An improved method for seismic moment tensor inversion of acoustic emissions through assessment of sensor coupling and sensitivity to incidence angle, *Int. J. Rock Mech. Min. Sci.*, **65**, 153–161.
- Kwiatak, G., Goebel, T. & Dresen, G., 2014b. Seismic moment tensor and b value variations over successive seismic cycles in laboratory stick-slip experiments, *Geophys. Res. Lett.*, **41**(16), 5838–5846.
- Li, B.Q. & Einstein, H.H., 2017. Comparison of visual and acoustic emission observations in a four point bending experiment on barre granite, *Rock Mech. Rock Eng.*, **50**(9), 2277–2296.
- Lockner, D., Walsh, J. & Byerlee, J., 1977. Changes in seismic velocity and attenuation during deformation of granite, *J. geophys. Res.*, **82**(33), 5374–5378.
- Maeda, N., 1985. A method for reading and checking phase times in auto-processing system of seismic wave data, *Zisin= Jishin*, **38**(3), 365–379.
- McEvelly, T. & Majer, E., 1982. Asp: An automated seismic processor for microearthquake networks, *Bull. seism. Soc. Am.*, **72**(1), 303–325.
- McLaskey, G.C. & Glaser, S.D., 2012. Acoustic emission sensor calibration for absolute source measurements, *J. Nondestruct. Eval.*, **31**(2), 157–168.
- McLaskey, G.C., Lockner, D.A., Kilgore, B.D. & Beeler, N.M., 2015. A robust calibration technique for acoustic emission systems based on momentum transfer from a ball drop, *Bull. seism. Soc. Am.*, **105**(1), 257–271.
- Metropolis, N., Rosenbluth, A.W., Rosenbluth, M.N., Teller, A.H. & Teller, E., 1953. Equation of state calculations by fast computing machines, *J. Chem. Phys.*, **21**(6), 1087–1092.
- Obert, L. & Duval, W., 1942. Use of subaudible noises for the prediction of rock bursts, Part II, Report of investigations (United States. Bureau of Mines). R.I. 3654.
- Ojala, I.O., Main, I.G. & Ngwenya, B.T., 2004. Strain rate and temperature dependence of Omori Law scaling constants of AE data: implications for earthquake foreshock-aftershock sequences, *Geophys. Res. Lett.*, **31**(24), doi:10.1029/2004GL020781.
- Ono, K., 2016. Calibration methods of acoustic emission sensors, *Materials*, **9**(7), 508.
- Pettitt, W.S., 1998. Acoustic emission source studies of microcracking in rock, *PhD thesis*, University of Keele.
- Schofield, B., 1961. Acoustic emission under applied stress, Tech. Rep. ARL-150, Lessells and Associates, Boston.
- Stanchits, S., Mayr, S., Shapiro, S. & Dresen, G., 2011. Fracturing of porous rock induced by fluid injection, *Tectonophysics*, **503**(1), 129–145.
- Swindell, W. & Snell, N., 1977. Station processor automatic signal detection system, phase i: Final report, station processor software development, *Texas Instruments Report No. ALEX (01)-FR-77-01, AFTAC Contract Number FO8606-76-C-0025, Texas Instruments Incorporated, Dallas, Texas*.
- Tang, X., Zhu, Z. & Toksöz, M., 1994. Radiation patterns of compressional and shear transducers at the surface of an elastic half-space, *J. acoust. Soc. Am.*, **95**(1), 71–76.
- Waldhauser, F. & Ellsworth, W.L., 2000. A double-difference earthquake location algorithm: method and application to the Northern Hayward Fault, California, *Bull. seism. Soc. Am.*, **90**(6), 1353–1368.
- Weemstra, C., Boschi, L., Goertz, A. & Artman, B., 2013. Seismic attenuation from recordings of ambient noise attenuation from ambient noise, *Geophysics*, **78**(1), Q1–Q14.
- Winkler, K., Nur, A. & Gladwin, M., 1979. Friction and seismic attenuation in rocks, *Nature*, **277**(5697), 528.
- Yoshimitsu, N., Furumura, T. & Maeda, T., 2016. Geometric effect on a laboratory-scale wavefield inferred from a three-dimensional numerical simulation, *J. appl. Geophys.*, **132**, 184–192.
- Zhang, H. & Thurber, C.H., 2003. Double-difference tomography: the method and its application to the Hayward Fault, California, *Bull. seism. Soc. Am.*, **93**(5), 1875–1889.

APPENDIX A: WAVEFORMS AFTER THE 3RD BOUNCING EVENT

In the main text, we only use waveform data for the first three bounces. We show the complete continuous waveforms containing waveforms after the third bounce event for 16 sensors in Fig. A1. The expected fourth bouncing event, marked as a dashed triangle, does not appear around the theoretical time, but around 0.2 s later. The fourth bouncing event even presents higher amplitude than the third bouncing event at sensor 4, 8, 12 and 16. This indicates that after the third bounce, when the rebound vertical velocity becomes 21.6 per cent of the initial velocity v_0 and the maximum rebound height becomes 4.9 mm (comparable to the radius of the ball 3.18 mm), the simple rebound model cannot predict the ball's motion. The inclusion of other forces neglected in the main text, for example, the drag force due to air resistance, and the Magnus force due to the ball's spin, and the buoyant force, may help to improve the simple rebound model and predict the ball's trajectory after the third bounce; however, that is beyond the scope of this paper.

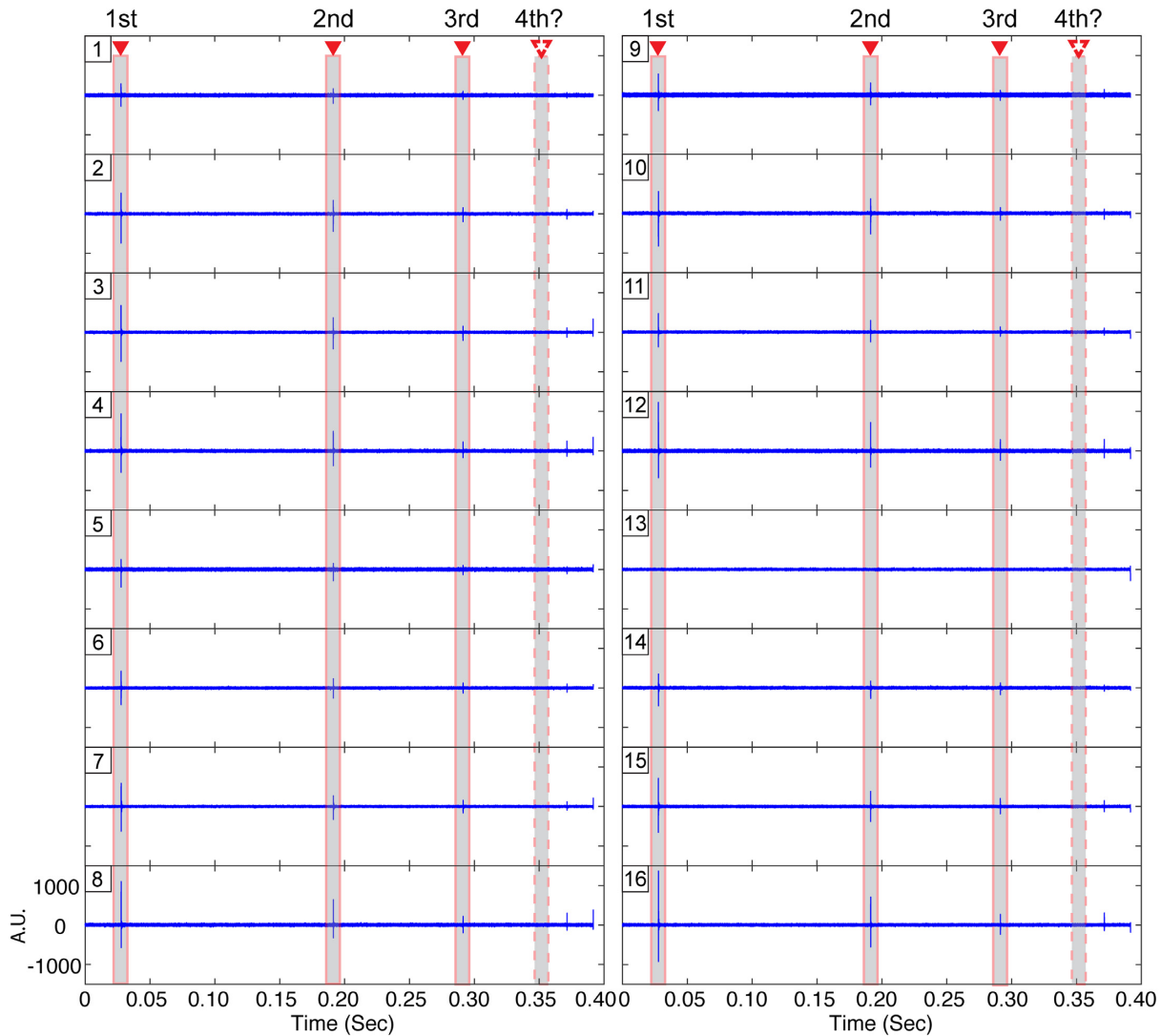


Figure A1. Complete continuous waveforms containing waveforms after the 3rd bounce event for 16 sensors. The first three bouncing events are denoted as solid red triangles. The dashed triangle marks the theoretical arrival time of bounces based on eq. (4).

APPENDIX B: DIRECTIONAL RESPONSE OF A SENSOR

We justify the cosine approximation of the directional response of a sensor in eq. (12) in this appendix. Tang *et al.* (1994) derived the radiation patterns of an elastic wave field generated by circular plane compressional and shear transducers. The amplitudes of generated compressional waves due to a compressional PZT sensor at a distance of R away from the sensor and an angle θ with the normal direction of the sensor surface is

$$u_R = \frac{R_s^2 \sigma_{zz} \exp(-ik_\alpha R)}{4\pi\mu R} \left[\frac{J_1(k_\alpha R_s \sin \theta)}{k_\alpha R_s \sin \theta} \right] \times \frac{(V_S/V_P)^2 \cos \theta [1 - 2(V_S/V_P)^2 \sin^2 \theta]}{[1 - 2(V_S/V_P)^2 \sin^2 \theta]^2 + 4(V_S/V_P)^3 \sin^2 \theta \cos \theta [1 - (V_S/V_P)^2 \sin^2 \theta]^{1/2}}, \quad (\text{B1})$$

where $R_s = 5$ mm is the radius of the PZT sensor, σ_{zz} is stress uniformly distributed on the surface of the piston surface of the PZT sensor, $V_P = 6011.6$ m s⁻¹ and $V_S = 3093.0$ m s⁻¹ are the com-

pressional wave velocity and shear wave velocity of the titanium sample of the compressional waves, k_α is the wave number of P wave.

If we assume the directional response of a sensor as a transmitter and receiver are equivalent, the theoretical radiation pattern in Tang *et al.* (1994) can be used to model the received amplitude as a function of incident angle. We compared the theoretical radiation pattern of compressional waves and the received amplitude as a function incident angle θ at frequencies of 100 kHz, 400 kHz, 700 kHz and 1 MHz in Figs B1 (a) and (b). The cosine dependence used in our paper is close to the theoretical solution at low frequency ($f = 100$ kHz). Kwiatek *et al.* (2014a) have used a bell-shaped function $h = \exp(-a\alpha^b)$ to model the angular dependence, which is close to the theoretical pattern at medium frequency ($f = 700$ kHz). More complex multilobe patterns appear at high frequency ($f = 1$ MHz). Because the dominant frequency of waveforms due to ball bounces is less than 100 kHz (Figs B1c and d), it is proper to use a cosine approximation.

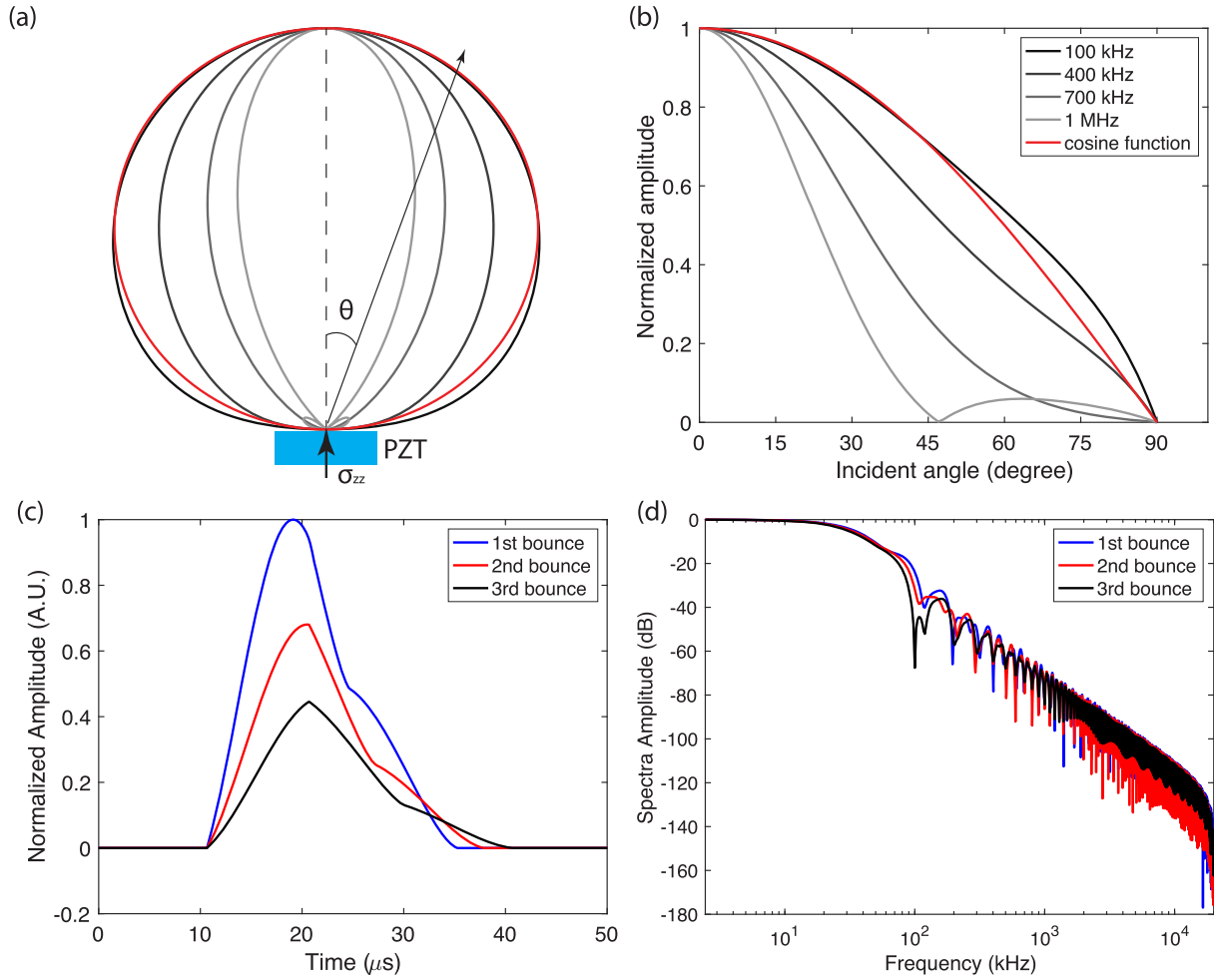


Figure B1. (a) The radiation pattern of compressional waves of a compressional PZT sensor at frequencies of 100 kHz, 400 kHz, 700 kHz and 1 MHz. The red line denotes the radiation pattern of the cosine approximation. (b) The received amplitude as a function of incident angle. The red line denotes the radiation pattern of the cosine approximation. (c) The normalized compressional waveforms due to ball bounces at sensor 1. (d) The normalized spectra amplitude of compressional waveforms due to ball bounces at sensor 1.

APPENDIX C: BOUNDARY EFFECTS ON WAVE PROPAGATION MODELLING

The Green's function in the main text is for an infinite unbounded homogeneous medium. To show that this approximation is valid for our experiment setup, we model the wave propagation in a more realistic environment using finite difference (FD) method with cylindrical coordinates. A cylindrical finite difference program is used to model the wave propagation in this ball drop system (Chen *et al.* 1998).

Fig. C1(a) shows the schematic of the FD model. A cross-section of the cylinder is plotted in colour. The green region denotes material 1, which is the ball drop apparatus. The blue region denotes material 2, which is the sample. The four red circles show the locations of sensors, which are the same locations relative to the loading force as sensors in the experiment. The loading force function is set to be a Ricker wavelet with a central frequency of 40 kHz.

To model the wave propagation for an infinite unbounded homogeneous space, we set both material 1 and material 2

to be Titanium ($V_p^{Ti} = 6011.6 \text{ m s}^{-1}$, $V_s^{Ti} = 3093.0 \text{ m s}^{-1}$ and $\rho^{Ti} = 4506.0 \text{ g cm}^{-3}$) or Granite ($V_p^{Gt} = 5616.0 \text{ m s}^{-1}$, $V_s^{Gt} = 3463.0 \text{ m s}^{-1}$ and $\rho^{Gt} = 2.75 \text{ g cm}^{-3}$), and add absorbing boundary conditions outside (orange region). The black lines in Figs C1(b) and (c) show the modelled waveforms for the baseline cases for Titanium and Granite samples with the infinite unbounded homogeneous approximation.

Then we set material 1 to be Steel ($V_p^{Steel} = 5525.8 \text{ m s}^{-1}$, $V_s^{Steel} = 2927.0 \text{ m s}^{-1}$ and $\rho^{Steel} = 8050.0 \text{ g cm}^{-3}$), which is the same as for the real experimental setup with the ball drop apparatus made of Steel. The received waveforms for the Titanium and Granite samples are shown in dashed red lines in Figs C1(b) and (c), compared with the relative corresponding infinite unbounded approximation. The waveforms are almost identical for the Titanium sample with or without the Steel–Titanium boundary. The waveform difference is more obvious for the Granite sample. This is because the impedance contrast between Granite and Steel is bigger than that between Titanium and Steel.

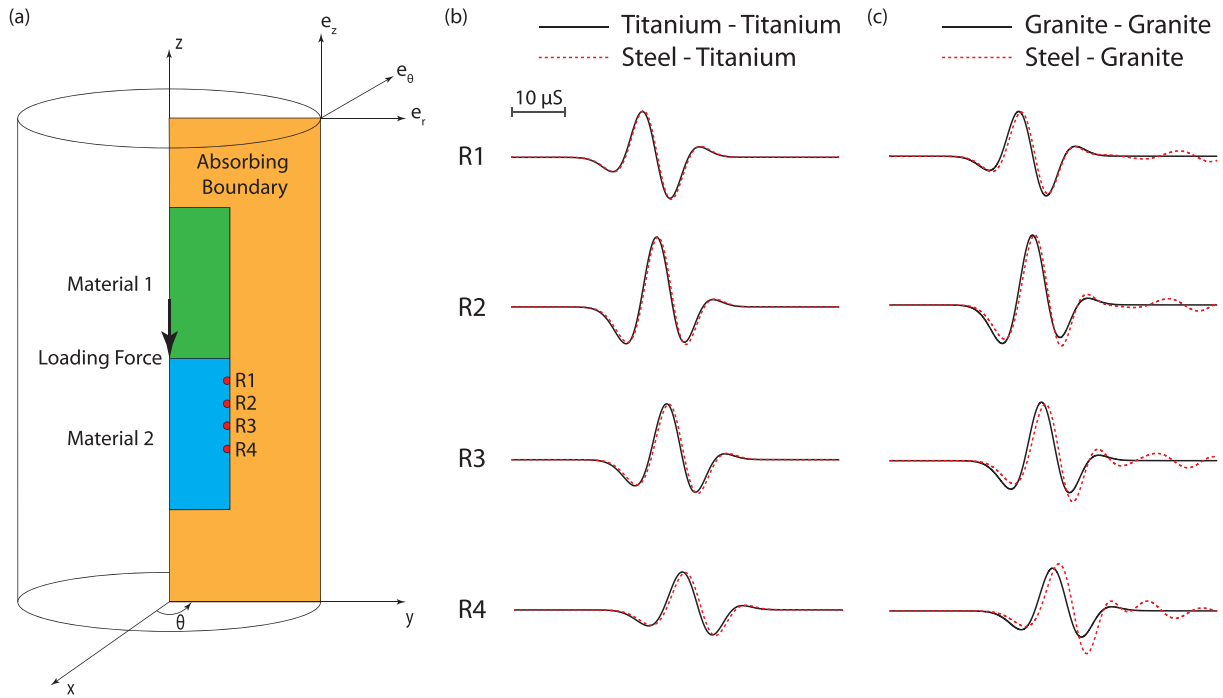


Figure C1. (a) A schematic of the finite difference model. The waveform comparison between the experimental setup with the ball drop apparatus made of Steel and the infinite unbounded homogeneous approximation at four receivers for (b) Titanium and (c) Granite samples.